Available online at www.sciencedirect.com
ScienceDirect
Journal of the European Ceramic Society 29 (2009) 3135–3146
www.elsevier.com/locate/jeurceramsoc

The crystalline-to-amorphous transition in shock-loaded mullite $Al_2{}^{VI}(Al_{2+2x}Si_{2-2x})^{IV}O_{10-x}$ in the light of shear modulus anisotropy

W. Braue [a,*], B. Hildmann [a], H. Schneider [b], U. Hornemann [c]

[a] German Aerospace Center (DLR), Materials Research Institute, Linder Höhe, D-51147 Cologne, Germany
[b] University of Cologne, Institute of Crystallography, Zülpicher Str. 49b, D-50674 Cologne, Germany
[c] Ernst Mach Institute, Fraunhofer Institute for High-Speed Dynamics, Am Christianswuhr 2, D-79400 Kandern, Germany

Received 10 March 2009; received in revised form 12 May 2009; accepted 30 May 2009
Available online 9 July 2009

Abstract

We present experimental evidence for shock-wave induced amorphization in polycrystalline and single crystal mullite, $Al_2{}^{VI}(Al_{2+2x}\,Si_{2-2x})^{IV}O_{10-x}$, at peak pressures above 35 GPa. The transition proceeds along with a network of very thin glass lamellae (planar deformation features (PDFs)) of mullite-normative composition extending parallel to low-index crystallographic planes including {1 2 0}, {2 3 0} and {1 1 0}. Cumulative microstructural evidence from the PDFs derived via analytical transmission electron microscopy suggests a shear-induced formation mechanism. Experimental PDFs match the relative minima of the calculated representation surfaces of the shear modulus suggesting that suitable PDF orientations can be derived from the elastic anisotropy of mullite. PDFs in mullite are in good agreement with those reported for naturally shocked sillimanite.

Unlike the formation of shear-induced PDF-type glass lamellae in shocked mullite, the thermal decomposition of mullite following high post-shock temperatures results in a fine-grained phase assemblage consisting of corundum plus amorphous silica, and represents the most abundant transformation mechanism in the shock regime investigated (20–40 GPa). No stishovite was observed. At shock levels beyond 35 GPa thermal decomposition of mullite may occur along with PDFs within the same specimen.

Keywords: Shock deformation; Electron microscopy; Plasticity; Mullite; Structural applications

1. Introduction

Dynamic compression of solid matter is a traditional domain of the geological science community where primary interest is directed towards the effects of shock metamorphism upon terrestrial crustal rocks and extraterrestrial impactites.[1–5] Notably the high strain rates released during shock loading bear a high potential for materials processing. Shock-assisted compaction has been employed successfully for the compaction of covalently bonded ceramic systems (e.g. SiC, BN, AlN, graphite, diamond) of high purity which are difficult to densify otherwise. During shock loading, different sources of energy dissipation such as friction, fracture and partial melting are released upon acceleration of the powder particles by the shock wave creating high dislocation densities and point defect concentrations.[6–11]

In response to shock-induced compression either in the laboratory or during a natural impact, crystalline constituents develop a variety of structural defects which are distinctively different from those introduced during static deformation[12–14]. With increasing pressure these characteristic defects include planar fracture, mechanical twinning, kink bands, mosaicism, and the so-called planar deformation features (PDFs) introduced via shock-induced amorphization.

PDFs define the most intriguing class of shock indicators. They consist of straight, narrow glass lamellae exhibiting the same chemical composition as the host crystal and have been described for a number of shock-loaded rock-forming minerals,[12,15–17] but as discussed in the present study, they may form in ceramic compounds as well. PDFs reflect elastic instabilities on specific closely packed crystallographic planes following the breakdown of the general Born stability criterion as defined by a positive definite matrix of the stiffness tensor c_{ij}, once a critical shock level has been exceeded.[18,19] While destabilization of some crystal lattices upon shock compaction

* Corresponding author.
E-mail address: wolfgang.braue@dlr.de (W. Braue).

0955-2219/$ – see front matter © 2009 Elsevier Ltd. All rights reserved.
doi:10.1016/j.jeurceramsoc.2009.05.051

may be accomplished without a shear component,[20] it is generally accepted that the very thin (of the order of ×10 nm) PDFs are formed by a shear process during dynamic compression.[21,22] These findings are in line with the general conception that even in uniaxial compression state shear is always effective on selected crystallographic planes. The PDF fine structure may be affected by post-shock annealing effects and in some systems frictional melting seems to be associated with PDFs.[23] The orientation of PDFs shows no pressure dependence. With increasing pressure, thickening of PDFs may yield extended areas of so-called diaplectic glasses.[22,24] It has been emphasized that accommodation of the compressed volume behind the shock front can only be achieved via regularly spaced lamellae of dense amorphous material.[20,22] Therefore PDFs must not be confused with amorphization of crystalline matter upon static compression.[25–27]

Although the shock response of Al_2O_3[28–30] and the Al_2SiO_5 polymorphs, particularly sillimanite, is well documented in the literature,[31,32] dynamic compression of ceramic compounds such as the alumosilicate mullite has only attracted attention in recent years.

The natural occurrence of mullite is rare. It was first reported in the early 1920s from a high-level intrusion of an Al-rich clay shale by a basaltic magma at the Isle of Mull in the Western Scottish Highlands.[33] Not surprisingly, naturally shocked mullite is presently unknown. However, the crystal structures of mullite and sillimanite are very similar suggesting that an in-depth comparison of the shock behavior of mullite derived in the laboratory with naturally shocked sillimanites will provide a more detailed assessment of the shock performance of this family of compounds.

Mullite, $Al_2{}^{VI}(Al_{2+2x}\ Si_{2-2x})^{IV}O_{10-x}$, $(0.17 < x < 0.50)$ has an oxygen-deficient orthorhombic structure with straight chains of edge-sharing $[AlO_6]$ octahedra extending parallel to the *c*-axis which are cross-linked by chains of doublets of $[(Si/Al)O_4]$ tetrahedra[34,35] (see also Section 4, Fig. 9 for a presentation of the mullite average structure). With the bulk composition ranging from nominally $3Al_2O_3{\cdot}2SiO_2$ ($x = 0.25$) to $2Al_2O_3{\cdot}1SiO_2$ ($x = 0.40$), mullite is the only stable phase in the binary system Al_2O_3–SiO_2 under normal conditions.

Apart from the fact that sillimanite features no oxygen vacancies, the structural differences between sillimanite and mullite are basically related to the site occupation factor of the aluminum and silicon atoms in the tetrahedral double chains. In sillimanite these are fully occupied in an ordered manner. In mullite they are only partially occupied (sites occupation factor ~0.8) in a random manner which gives rise to bisection of the *c*-parameter. Moreover, sillimanite lacks the partially occupied tetrahedral chains extending parallel to the *c*-axis which involve the T^* sites with site occupation factors ~0.2.

First results on shock-induced phase transitions of polycrystalline mullite including (i) the formation of planar deformation features as well as (ii) the thermal decomposition of mullite were reported in 1995.[36] Recently, the Hugoniot elastic limit of polycrystalline mullite was determined experimentally to be 16.1 GPa[37] which compares well to the Hugoniot elastic limit of sapphire (12–20 GPa[28]) for different crystallographic orientations. A phase transition in mullite occurring at 30.4 GPa was reported[38] while at 40 and 49 GPa, mullite nanocrystals were found to be embedded in a non-crystalline phase. Exposure to still higher shock pressures above 65 GPa resulted in complete decomposition of mullite to form a very fine-grained mixture of γ-alumina and amorphous silica.

The previous shock data for mullite still leave a variety of open issues and inconsistencies within the literature which are addressed in the present paper. The main focus of this study is directed towards the assessment and interpretation of planar deformation features observed in polycrystalline and single crystal mullite materials as compared to mullite's close structural relative sillimanite. The concept of a shear-induced formation process for PDFs proven successfully for a number of shock-loaded rock-forming minerals[21] is extended to the mullite system employing sillimanite for benchmarking. It will be shown that the formation of PDFs in mullite planes can indeed be rationalized via the elastic anisotropy of mullite and match with the ensemble of PDFs reported from naturally shocked sillimanite.[31] The thermal decomposition of mullite introduced by the high post-shock temperatures represents the second transformation mechanism of shocked mullite and is discussed complementary to shock-induced amorphization.

2. Experimental procedure and materials

2.1. Shock recovery experiments

The shock experiments were performed at the Ernst Mach Institute, Freiburg, Germany by planar impact techniques[2,13] in the 20–40 GPa pressure range. The experimental setup is depicted in Fig. 1a. The specimen was loaded in a cylindrical ARMCO (American Rolling Mill Company)-type iron sample container surrounded by intercalated steel plates which serve as momentum traps. Dynamic compression was achieved through a steel flyer plate accelerated by an explosive device. The flyer plate was resting on a spacer ring. Upon impact of the flyer plate on the upper sample container surface a plane shock wave was transmitted into the specimen. The specimens consisted of thin polished mullite sections, typically 0.5 mm thick and 10 mm in diameter, which were embedded in NaBr in order to suppress rarefaction waves from the lateral and bottom surfaces of the sample container (Fig. 1b).

Peak pressures transmitted into the samples could be varied by using different types of explosives and/or by modifying the thickness of the flyer plate, respectively. Peak pressures were determined by separate calibration tests using the pin contactor technique via measuring the free surface velocity at the upper container/sample interface as discussed elsewhere.[13] The pressure in the mullite sample was determined by impedance matching in a multiple reflection mode using the Hugoniot data of ARMCO-iron. Upon shock-loading the sample container is usually slightly deformed at the impact surface. At pressures above 30 GPa recovery of specimens for TEM preparation becomes progressively difficult due to complete fragmentation of the mullite materials and/or strong adhesion to the container material.

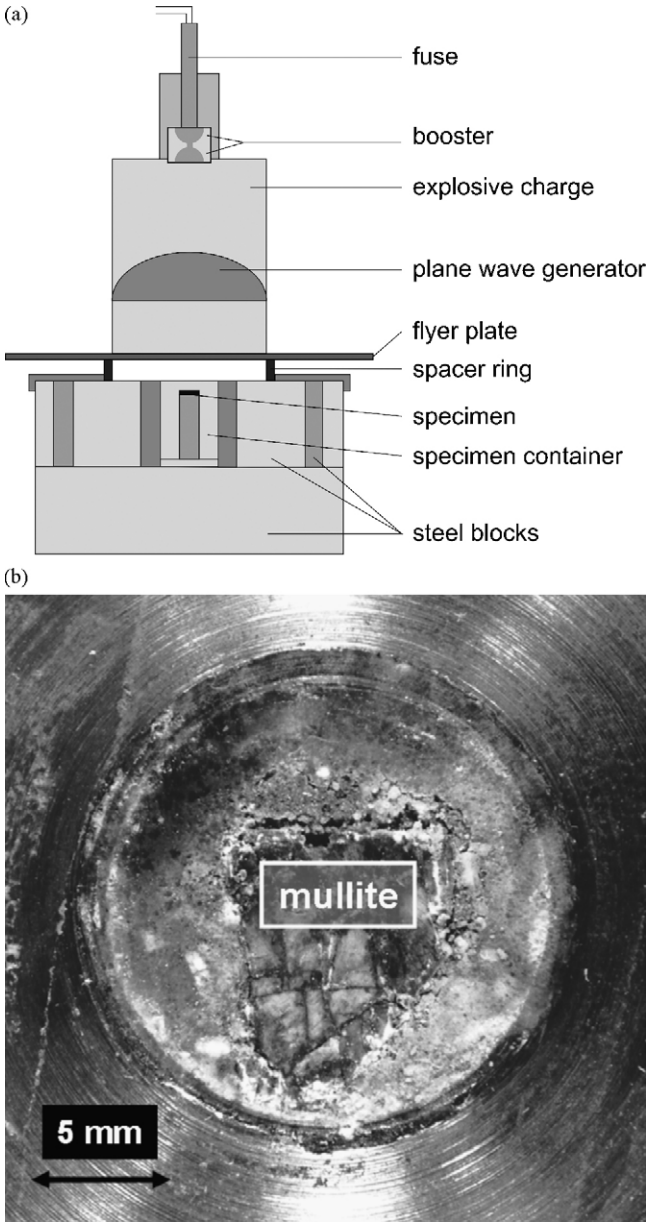

Fig. 1. (a) Experimental setup (schematic) employed for the shock recovery experiments. (b) Plane view of the sample container borehole holding a shocked single crystal mullite specimen embedded in NaBr.

2.2. Starting materials, characterization upon shock recovery

Three different synthetic mullite materials were employed in this study: (i) a coarse-grained polyphase fused 2/1 mullite refractory brick, (ii) (0 0 1) sections from a Czochralski-grown 2/1 mullite single crystal, and (iii) a very fine-grained sintered polycrystalline 3/2 mullite ceramic material.

The 2/1 mullite crystals of the fused mullite brick, some 10 μm in grain size, were located between large porous corundum laths and a continuous siliceous glassy phase holding numerous zirconia particles. The non-crystalline phase acted as a sink for impurities such as sodium, calcium and iron. Due to the abundance of corundum in the fused mullite brick, shock deformation features of corundum[29] were analyzed and compared to mullite. Directions $[u\,v\cdot w]$ in corundum electron diffraction patterns refer to the 3-axis, 3-index Miller notation containing the redundant dot symbol for fast recognition.

The sintered 3/2 mullite ceramic exhibited an average grain size of 1 μm and was employed in order to address possible effects of very small grain sizes on shock-induced microstructures.

Specimen fragments recovered from the shock experiments were embedded in epoxy glue and thinned by dimpling and standard argon-ion beam techniques. In most cases TEM specimens were sampled with the foil normal approximately parallel to the main direction of the primary shock wave. This might not be true for heavily fragmented and tilted specimen areas and/or deviatoric shock-wave components being effective during the shock experiment.

A FEG TEM/STEM operating at 300 kV acceleration voltage (Tecnai F 30 ST, FEI Instruments, The Netherlands) was employed in the research. Phase analysis was performed via selected area electron diffraction (SAD), convergent beam electron diffraction (CBED), and small probe X-ray microanalysis (EDS).

3. Results

3.1. Shock-induced mosaic structures and the formation of planar deformation features (PDFs) in mullite

Upon shock loading at 20 GPa the mullite materials were found to be devoid of shock-induced phase transformation or decomposition reactions. The individual mullite grains however disintegrated into numerous domains (“mosaicism”) separated by subgrain boundaries. This is considered a defect structure typical for rather moderate shock pressures[2] which may be associated with brittle failure, independently of the nature of mullite starting material. Typical mosaicism from a (0 0 1) single crystal specimen is depicted in Fig. 2. The subgrain boundaries

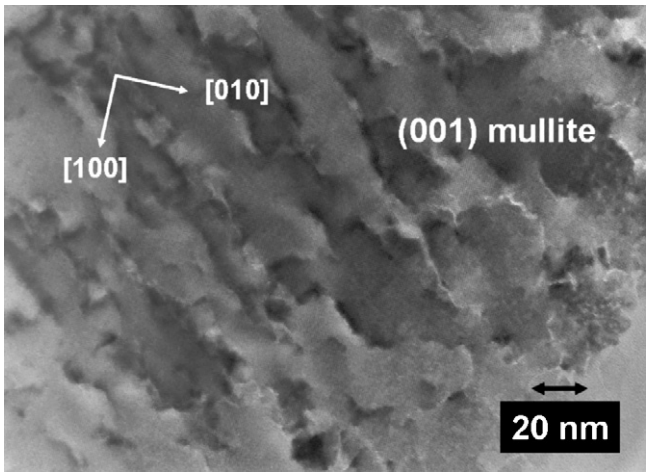

Fig. 2. Subgrain boundaries in shock-loaded (0 0 1) single crystal mullite (20 GPa) due to slight deviations of mullite domains (“mosaicism”) from the common [0 0 1] zone axis orientation (TEM, bright field (BF)).

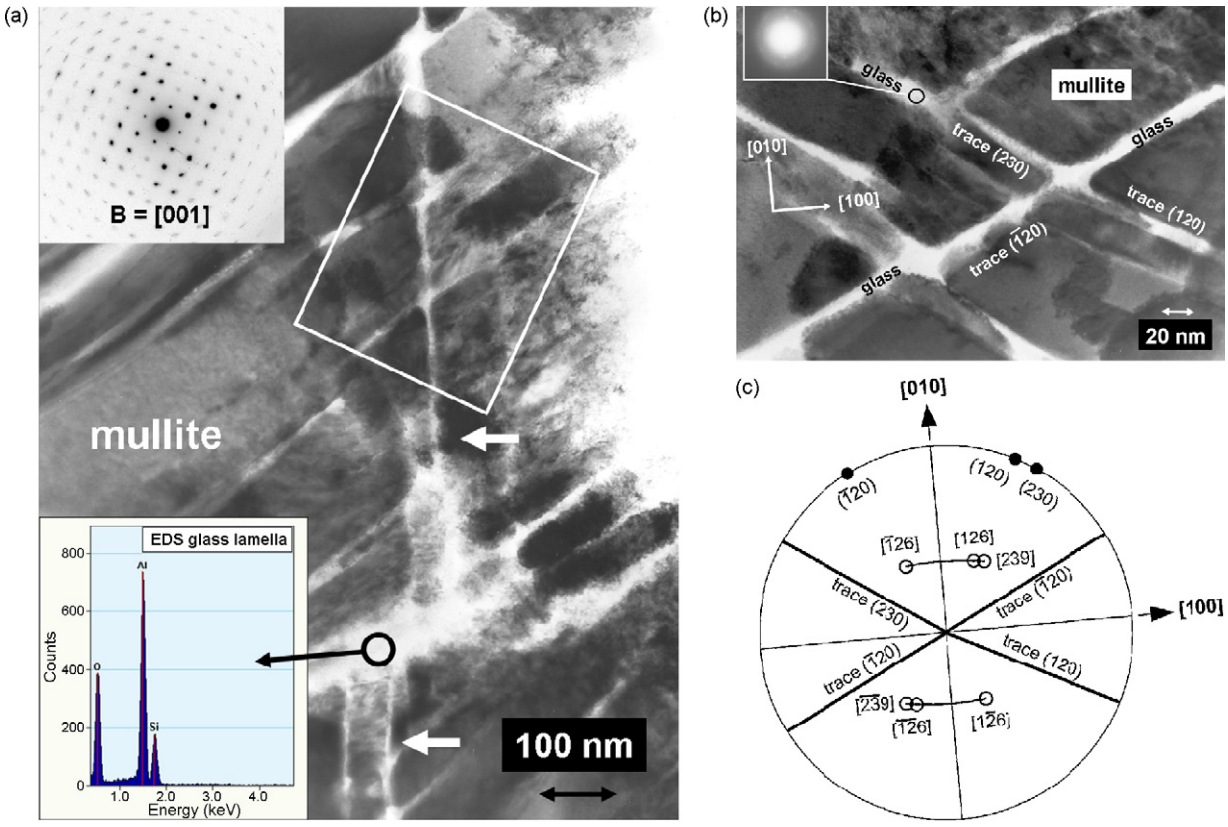

Fig. 3. (a) Network of non-crystalline lamellae (PDFs) in mullite grain from fused-mullite refractory brick upon shock loading at 35 GPa (TEM, BF). Quantitative analysis of EDS spectra collected from non-crystalline areas (circle symbol) indicated a mullite-normative composition. Local displacement of intersecting PDFs upon shear is highlighted by white arrows. (b) HREM image of boxed region in (a). PDF lamellae are oriented edge-on and extend parallel to (1 2 0), ($\bar{1}$ 2 0) and (2 3 0) planes, respectively. A CBED pattern collected from a PDF is displayed in the inset emphasizing its amorphous nature. (c) Analysis of crystallographic directions of the relevant shock waves giving rise to the simultaneous formation of shear-induced PDFs parallel to (1 2 0), ($\bar{1}$ 2 0) and (2 3 0) mullite planes (b). Their poles and traces (bold lines) are plotted in the mullite (0 0 1) standard stereographic projection which has been rotated into coincidence with the corresponding TEM bright field image (b).

Following Mohr's construction PDFs on (1 2 0), ($\bar{1}$ 2 0) and (2 3 0) planes are related to shock-wave directions [1 2 6], [$\bar{1}$ 2 6] and [2 3 9], respectively, which can be rationalized via decomposition of a single shock wave.

may extend into numerous nanoscale microcracks which merge into a general [1 1 0] texture. At other locations of the specimen large cracks emerged from pronounced lattice compression sites characterized by the typical strain whorls observed in diffraction contrast. Dislocation networks were rarely observed. Although brittle fracture in shocked compounds may be crystallographically controlled, planar fractures or cracks parallel to the preferred cleavage plane of mullite (0 1 0) were not observed.

At shock pressures exceeding 20 GPa the general microstructure changed significantly. Shock-induced amorphization is introduced in the following while thermal decomposition is discussed in Section 3.2. At 35 GPa the mullite microcrystal displayed in Fig. 3a exhibited a very obvious series of straight and narrowly spaced planar defects. It is noteworthy that orienting these features edge-on required some 40° drum tilt off the foil normal of the TEM specimen which originally extended parallel to the direction of the primary shock wave. This observation held important implications with respect to the verification of a shear component being active during shock compaction (see below). Upon closer inspection via HREM and microdiffraction the planar features proved to be an intersecting network of thin amorphous lamellae. EDS spectra collected from the lamellae and the adjacent crystalline mullite area yielded virtually the same normative mullite composition. Thus, the lamellae were clearly identified as PDFs.[2,5,12] In most cases the PDFs were straight, but appeared slightly curved in thicker regions of the specimen. Fig. 3b displays a HREM image of the mullite microcrystal from Fig. 3a in [0 0 1] orientation. The PDFs are oriented edge-on and extend parallel to the traces of $\{h\,k\,0\}$-type prism planes including the (1 2 0), ($\bar{1}$ 2 0) and (2 3 0) planes. Lamellae displacement due to shearing was observed for intersecting PDFs, as highlighted by arrows in the center of Fig. 3a. Typically, PDF thickness was of the order of 10–15 nm. Most likely their true thickness was distinctly less. Mullite is known to be very prone to electron-beam induced radiation damage which imposed a notable broadening effect on PDFs within minutes of TEM inspection. Great care must be taken not to confuse artificial amorphization introduced via prolonged radiation damage with true areas of shock-induced glasses.[24] Leaving aside the first signs of radiation damage, Fig. 3a and b represent the early stage of shock-induced amorphization in mullite.

The shear character of the observed PDFs on mullite planes may be conveniently rationalized by applying Mohr's circle. Thus, shear stresses within a plane will be maximal if this plane

is tilted by 45° to the compression direction, therefore initiating PDFs. Note that this scenario exactly corresponded to the necessary tilting of the TEM specimen for edge-on imaging of the PDFs in Fig. 3b. Consequently, possible crystallographic directions of the relevant shock waves introducing the experimentally observed PDF could be derived from stereographic projections as shown in Fig. 3c for the polycrystalline mullite specimen (see Fig. 4c for the single crystal mullite case as discussed below). For convenience, the stereographic projections (Figs. 3c and 4c) were rotated into coincidence with the corresponding real space images with the PDFs oriented edge-on (Figs. 3b and 4b). Due to the appearance of non-symmetric equivalent PDFs, at least in Fig. 3b, different shock-wave directions must have been active during PDF formation. In Fig. 3c the shock-wave component parallel to [2 3 9] which gave rise to PDFs on {1 2 0} planes is 46.7° off the [0 0 1] direction. On the other hand, [1 2 6] related to PDFS on the (2 3 0) plane is off by 44.7°, both in good agreement with Mohr's circle. These different direction vectors could be considered as components of a single primary shock wave upon transformation. Their common location lies on the great circle segment of the plane they span in the corresponding stereographic projections.

Shock-induced formation of PDFs in mullite single crystal was investigated for a (0 0 1) specimen at 40 GPa only. A network of PDFs extending parallel to {1 1 0} planes is displayed in Fig. 4a. A HREM image of the boxed region is displayed in Fig. 4b. Apart from {1 1 0} no other family of PDFs was derived from the (0 0 1) specimen. As shown in the stereographic projection (Fig. 4c), Mohr's circle applied to this scenario yields [3 3 11] as the relevant shock-wave direction, 45.5° off the [0 0 1] direction.

3.2. Shock-induced thermal decomposition of mullite

The second transformation observed in shock-loaded mullite, for both the polycrystalline and the single crystal starting material, involved the decomposition of individual mullite grains to form α-Al_2O_3 and amorphous silica. No stishovite was observed as stated elsewhere for similar experiments.[37] Within the pressure range investigated (20–40 GPa) thermal decomposition represented the dominant type of microstructural response of mullite to shock loading. Once the shock level has exceeded 35 GPa, it may even occur simultaneously with the formation of PDFs within the same specimen.

For a single crystal mullite (0 0 1) substrate shocked at 30 GPa (Fig. 5a), the shock-induced breakdown of mullite to a newly formed alumina plus amorphous silica phase assemblage was found to be restricted to a small fine-grained transformation zone. The SAD diffraction pattern (see inset in Fig. 5a) collected from the transformed area revealed strong corundum {1 1 · 3} and {0 3 · 0} Debye Scherrer rings (among others) superimposed on (0 0 1) mullite reflections. No crystalline silica polymorph could be detected. Silica must be present in the amorphous state as EDS spectra collected from corundum-rich locations did always depict a distinct Si Kα signal.

On a local scale the fine-grained corundum plus amorphous silica phase assemblage may develop a strong texture

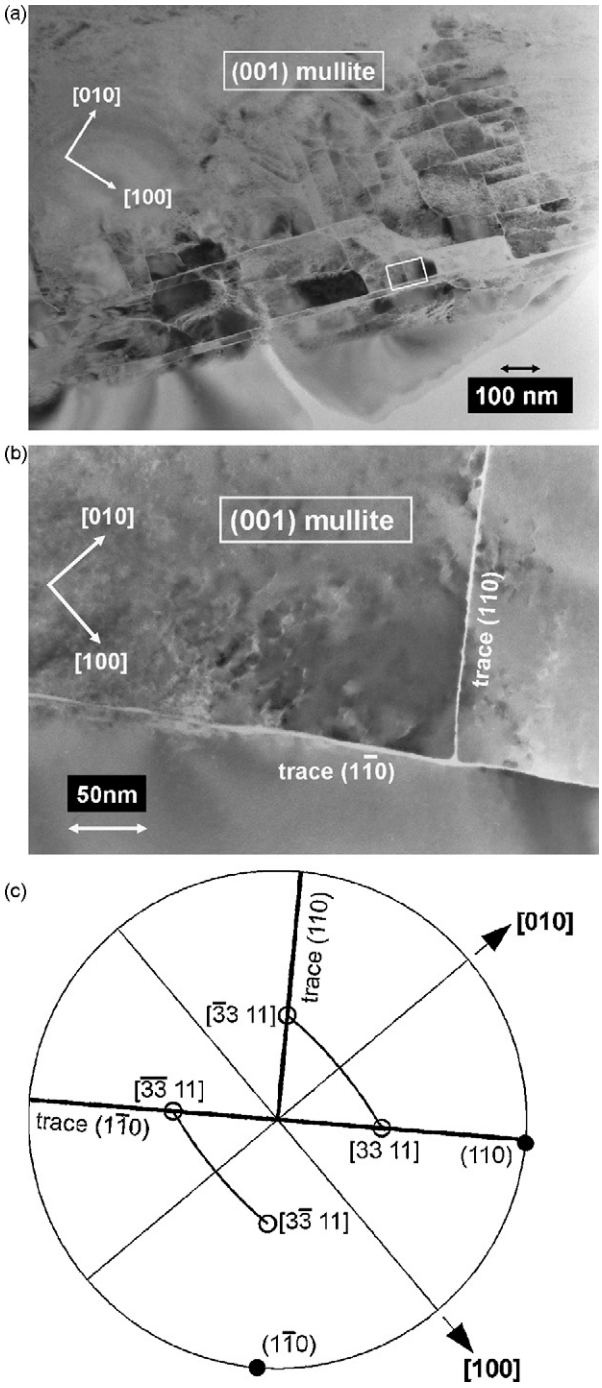

Fig. 4. (a) PDFs extending parallel to {1 1 0} planes in (0 0 1) single crystal mullite upon shock-loading at 40 GPa (TEM, BF). (b) HREM image of boxed region in (a). The glass lamellae are oriented edge-on exhibiting a thickness variation between 1.5 and 4.5 nm. (c) Analysis of the crystallographic direction of the relevant shock wave giving rise to the formation of shear-induced PDFs parallel to {1 1 0} mullite planes (a). Their poles and traces (bold lines) are plotted in the mullite (0 0 1) standard stereographic projection which has been rotated into coincidence with the corresponding TEM bright field image (b).
Following Mohr's construction relevant shock-wave directions for the {1 1 0}-type PDFs include [$\bar{3}$3 11] and [3 3 11] which can be rationalized via decomposition of a single shock wave.

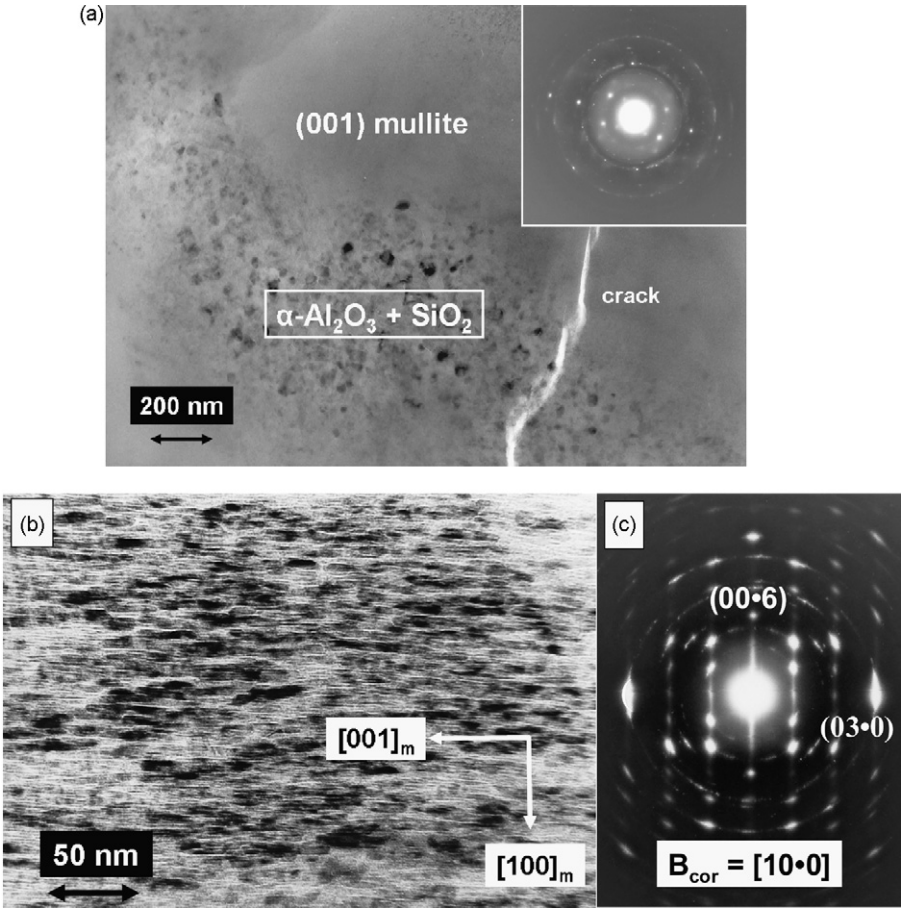

Fig. 5. (a) Local transition of (0 0 1) single crystal mullite to corundum and amorphous silica upon shock deformation at 30 GPa (TEM, BF). The composite SAD pattern inserted reveals strong corundum $\{1\,1\cdot3\}$ and $\{0\,3\cdot0\}$ Debye Scherrer rings (among others) superimposed on [0 0 1] mullite reflections. (b and c) Thermal decomposition of shock-loaded single crystal (0 1 0) mullite specimen (40 GPa) yielding a highly textured ⟨corundum plus amorphous silica⟩ phase assemblage, (b) defocused BF image (referring to the specimen orientation prior to the shock experiment), (c) corundum SAD pattern ($B = [1\,0\cdot0]$) from ⟨corundum plus amorphous silica⟩ phase assemblage. Note pronounced streaking in the diffraction pattern parallel to $[0\,0\cdot1]$ which corresponds to the needle-shaped grain morphology of the corundum grains extending parallel to the original mullite [0 0 1] direction in real space (b).

yielding a single crystal-type corundum SAD pattern which is believed to be related to pressure gradients within the specimen. Inhomogeneous pressure distribution is a common feature reported from shocked ceramic compounds giving rise to grain rotation and strong textural effects within the specimen.[6] This effect was demonstrated for a single crystal mullite (0 1 0) section exposed to 40 GPa shock pressure (Fig. 5b). Corundum was tilted to a $[1\,0\cdot0]$ zone axis orientation with elongated nanocrystals exhibiting grain dimensions of the order of 10 nm × 30 nm. Note the pronounced streaking parallel to $[0\,0\cdot1]$ in the diffraction pattern (Fig. 5c) which is due to the needle-shaped corundum grain morphology extending parallel to the original mullite [0 0 1] direction in real space (Fig. 5b). Numerous phase boundaries filled with amorphous silica become visible in the transformed region upon defocusing the objective lens. Considering the original mullite orientation prior to thermal decomposition, similar [0 1 0]//$[1\,0\cdot0]$ and [1 0 0]//$[0\,0\cdot1]$-type mullite/corundum orientation relationships as described elsewhere[39] were locally established in shocked mullite crystal.

Shock compression of the fine-grained sintered mullite ceramic at 35 GPa resulted in thermal decomposition of mullite only (Fig. 6). On a nanometer scale the clustered arrangement of the corundum plus amorphous silica-rich phase assemblage seemed to follow the grain texture of the starting material prior to shock deformation. No evidence for PDFs was derived from this experiment.

At 35 GPa the corundum grains from the fused mullite brick exhibited shock-induced basal twin lamellae, as shown in Fig. 7. Corundum orientation is parallel to $[1\,1\cdot0]$ thus imaging the basal plane twins edge-on. The corresponding SAD pattern (see inset in Fig. 7) is a mixture of fundamental $[h\,h\cdot0]$ spots, basal twin spots and overlapping matrix/twin reflections. No PDFs were observed in corundum, in agreement with previous research.[29,30]

4. Discussion

Microstructural and crystallographic evidence from PDFs in mullite suggested that the crystalline-to-amorphous phase tran-

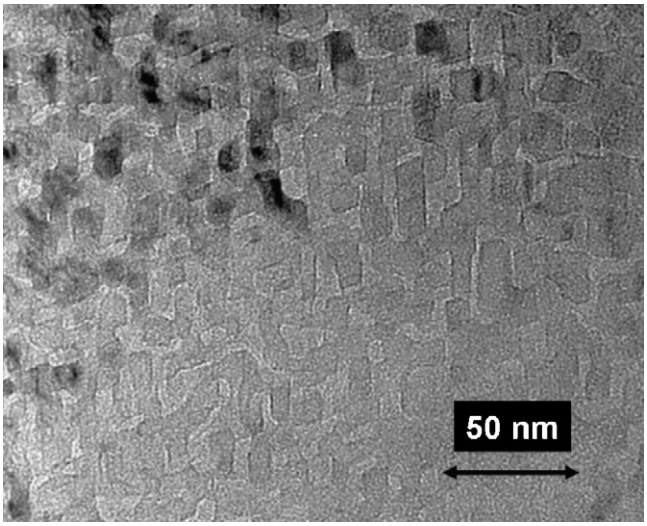

Fig. 6. Thermal decomposition of a former mullite grain (original grain size approximately 1 μm) from the fine-grained sintered 3/2 mullite starting material upon shock-loading at 35 GPa (TEM, BF). Numerous nanoscale alumina grains are incorporated in a siliceous amorphous phase.

sition was introduced by a shear component during dynamic compression. In their classic case study on quartz, Goltrant et al.[21,22] showed that the shear modulus decreased with increasing pressure and discontinuities giving rise to PDFs appeared on the $\{1\,0\cdot n\}$ type-rhombohedral planes ($n = 1, 2, 3, 4$) above a shock level of 10 GPa.

Although the Born stability criteria for the orthorhombic case was reported in a general, yet not fully expanded analytical expression,[40] a similar estimate on the limiting shock pressure in mullite cannot be accomplished as the pressure dependence of the elastic stiffness coefficients c_{ij} is currently unknown for mullite and sillimanite as well. If, however, the pressure dependence is neglected as a first approximation, calculation of the anisotropy of mullite's shear modulus at normal conditions (see Appendix A) with simultaneous consideration

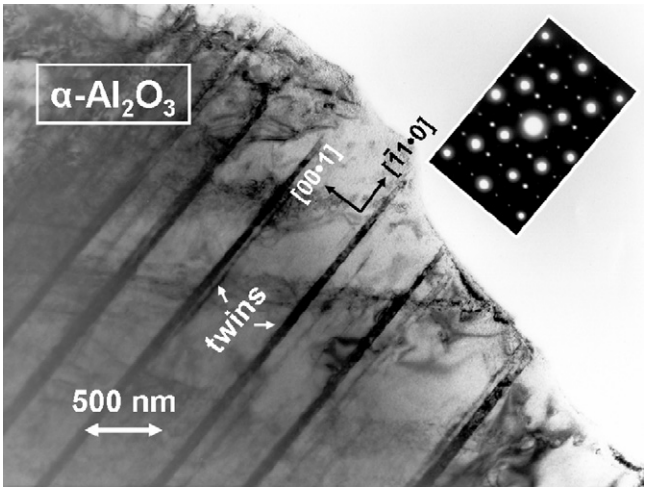

Fig. 7. Deformed corundum grain from the fused-mullite brick material displaying basal plane twinning upon shock loading at 35 GPa (TEM, BF). The electron beam is parallel to the $[1\,1\cdot 0]$ zone axis (see inset) thus imaging the twins edge-on.

Table 1
Elastic coefficients of 2/1 mullite and sillimanite[41,42] single crystals at room temperature employed in the calculation of shear modulus anisotropy. Elastic stiffnesses c_{ij} and elastic compliances s_{ij} are given in Voigt notation (see Appendix A).

Composition $Al_{4+2x}Si_{2-2x}O_{10-x}$	2/1-Mullite ≈ $2Al_2O_3{\cdot}SiO_2$, $x = 0.385$	Sillimanite, $Al_2O_3{\cdot}SiO_2$, $x = 0.0$
c_{11} [GPa]	291.3	287.3
c_{22}	232.9	231.9
c_{33}	352.1	388.4
c_{44}	110.3	122.4
c_{55}	77.39	80.7
c_{66}	79.90	89.3
c_{12}	112.9	94.7
c_{13}	96.22	83.4
c_{23}	121.9	158.6
s_{11} [TPa^{-1}]	4.314	4.042
s_{22}	5.995	6.515
s_{33}	3.540	3.590
s_{44}	9.066	8.170
s_{55}	12.922	12.392
s_{66}	12.516	11.198
s_{12}	−1.801	−1.467
s_{13}	−0.556	−0.269
s_{23}	−1.584	−2.346

of the specific planes relevant for PDFs is quite similar to the approach employed in[21] for addressing shear instabilities on selected quartz planes. Extrapolation to actual shock regimes limits the applicability of the shear modulus anisotropy in mullite to a qualitative argument, but as discussed in the following it is nevertheless suited to address shear instabilities on specific mullite planes.

The elastic stiffness coefficients c_{ij} of mullite employed in the calculation of shear modulus anisotropy are compiled in Table 1 in comparison with the sillimanite data from the literature.[41,42] Considering the close structural relationship between mullite and sillimanite the similarity between the corresponding elastic stiffness coefficients is not surprising. Mullite and sillimanite share high longitudinal stiffness coefficients c_{33} caused by load-bearing continuous tetrahedral and octahedral chains extending parallel to the c-axis. The softer octahedral chains[41–44] stabilize the tetrahedral chains against tilting and vice versa. Such continuous chains do not exist perpendicular to the c-axis. Therefore, the longitudinal stiffness coefficients c_{11} and c_{22} are significantly lower than c_{33} which can be rationalized by the alternating sequences of soft octahedral and hard tetrahedral units arranged in any direction perpendicular to the c-axis. The c_{11} coefficient exceeds c_{22} because the octahedral Al–O bonds are more compliant parallel to the b-axis than to the a-axis.

Shear stiffness coefficients of mullite increase in the sequence $c_{55} < c_{66} < c_{44}$ reflecting increasing resistance against shear deformation within the planes (0 1 0), (0 0 1) and (1 0 0), respectively. The shear stiffness coefficients of mullite are lower than those in sillmanite as the partial substitution of silicon by aluminium and initiation of oxygen vacancies via $2Si^{4+} + O^{2-} \rightarrow 2Al^{3+} + \square$ (oxygen vacancies □) causes a reduction of the mean tetrahedral bond strength.

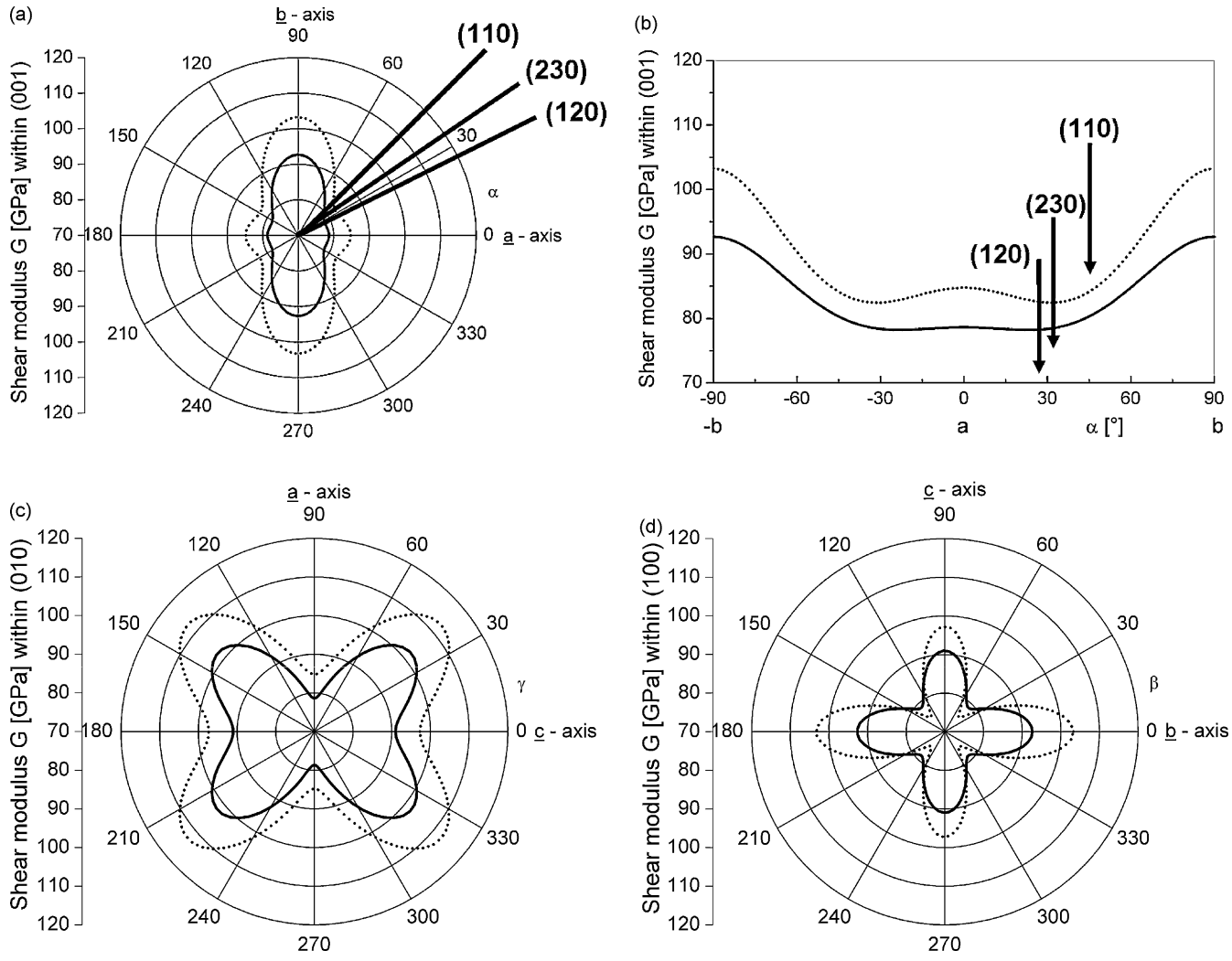

Fig. 8. Sections through the representation surfaces of the shear modulus G (l) in single crystal mullite (Table 1, solid line) in polar (a, c, d) and Cartesian coordinates (b), respectively. Sillimanite (Table 1, dotted line) is shown for comparison. Zero points are suppressed. (a, b) Central (0 0 1) section. Note the distinct relative minima of G (l) at approximately $\pm 30^\circ$ off the a-axis, in agreement with the traces of the experimentally observed PDFs (bolt lines) in mullite. (c) Central (0 1 0) section. Note the distinct relative minima of G (l) oriented parallel to ⟨1 0 0⟩ and ⟨0 0 1⟩. (d) Central (1 0 0) section. Note the distinct relative minima of G (l) oriented parallel to ⟨0 1 1⟩.

Given the elastic stiffness coefficients c_{ij} (Table 1) the shear modulus for the orthorhombic phase mullite was calculated from Eq. (1) as derived in the appendix. The three-dimensional representation surface of the shear moduli is conveniently depicted through the central (0 0 1), (0 1 0) and (1 0 0) sections, as shown in Fig. 8a, c and d in polar and in Fig. 8b in Cartesian coordinates, respectively. Here, the length of the radius vector in the direction of the unit vector l is proportional to shear modulus $G(l) = 1/s_{ij}(l)$ for arbitrary directions $l = (l_1, l_2, l_3)$ with the elastic compliance coefficients s_{ij}. Zero points in Fig. 8a–d are suppressed in order to highlight the relative changes of $G(l)$. As shown in Fig. 8a and b, the traces of the PDFs on $(h\,k\,0)$ planes match the relative minima within the (0 0 1) plane of the calculated representation surface of the shear modulus $G(l)$ indicating that the formation of PDFs complies with the soft modes in the shear modulus. From numerous planar features characterized by optical microscopy in naturally shocked sillimanite crystals, Stoeffler[24] found PDFs most frequently on $\{h\,k\,0\}$ prism planes including (1 1 0), (1 2 0), (1 3 0), (2 3 0) and (3 2 0) and less frequently on $\{h\,k\,l\}$bipyramid planes and (0 1 0)-type prism planes. Thus, the agreement in PDF-orientation between mullite and sillimanite is evident. The distinct relative minima in the (0 1 0) and (1 0 0) sections of the representation surface of the shear modulus as shown in Fig. 8c and d suggest that additional sets of PDFs may occur in shocked mullite which were not accessible in our experiments.

Other than the formation of PDFs, the thermal decomposition of shocked mullite represents a typical phenomenon known from shocked ceramic systems controlled by high post-shock temperatures during the decompression phase of the shock experiment.[13] As emphasized previously[2] post-shock temperatures exceeding the decomposition-, melting- and even vaporization temperatures of solid compounds may occur on pressure release from all shock states. Thermal decomposition of shocked mullite to form an intimate mixture of

alumina and amorphous silica is actually enhanced by the effects of high pressures due to the decrease in molar volume involved.

While our results on shock-induced transformations of mullite provide a consistent pattern of the interplay of PDF formation and thermal decomposition above 35 PGa, they do not comply with recent studies on polycrystalline shocked mullite.[37,38,45–48] Kawai et al.[37] claimed thermal decomposition of mullite to form corundum and stishovite at 30.4 GPa. This finding has not been verified via microstructural analysis but derived indirectly by fitting the cusps in their p–V mullite Hugoniot curve with shock data from the corundum plus stishovite phase assemblage which usually forms upon decomposition of kyanite Al_2SiO_5. Shock recovery experiments from the same group extended to 49 GPa yielded mullite and a considerable amount of non-crystalline phase in the X-ray diffraction patterns.[38] Unfortunately amorphization of mullite is addressed qualitatively only with no detailed crystallographic information furnished, so the significance of the microstructures displayed (Figs. 2 and 3 in ref. 38) is difficult to comprehend.

Furthermore, it has been argued that a shock induced crystalline-to-amorphous transition in mullite may be enhanced by some sort of phase instability related to the oxygen vacancies.[38] Moreover this instability should give rise to distinct microstructural differences in shock-loaded mullite as compared to sillimanite, as stated recently.[43] However, our results provided no significant microstructural differences between the shock response of mullite as compared to the published data on sillimanite.[24] While it is true that oxygen vacancies may contribute to a relative overall reduction of both longitudinal and shear stiffness in mullite as compared to sillimanite, the well documented PDFs in shocked sillimanite[31] which is devoid of oxygen vacancies clearly prove that they are not related to PDF formation. This study and previous related work[41,42] indicate that it is the interaction of all structural units in the mullite structure and less likely the effect of randomly distributed point defects such as oxygen vacancies which give rise to the anisotropy of the shear modulus in mullite. Notably the $[AlO_6]$ octahedra present the softest structural units during compression of Al_2SiO_5 polymorphs.[44] Our present study emphasizes that they are most compliant against shear as well. As highlighted in the [0 0 1] projection of the mullite average structure (Fig. 9), the high density of octahedra located on mullite planes {1 1 0}, {1 2 0}, {2 3 0} holding PDFs may furnish a supplementary structural argument for the calculated minimal values of the shear modulus (Figs. 8a and b) and the propensity of mullite to shock-induced amorphization.

Furthermore, the argument that amorphization of mullite may be induced by the kinetic hindrance of the thermal decomposition reaction[38,46] is in disagreement with our observation that PDF formation and thermal decomposition of mullite may occur within the same specimen at shock levels beyond 35 GPa. The abundance of corundum over transition aluminas (e.g. γ-Al_2O_3, δ-Al_2O_3) in our experiments which would rather be expected in the reaction mullite → alumina + silica, is explained via high post-shock temperatures (1000 °C estimated) exceeding the stability range of transition aluminas.[49]

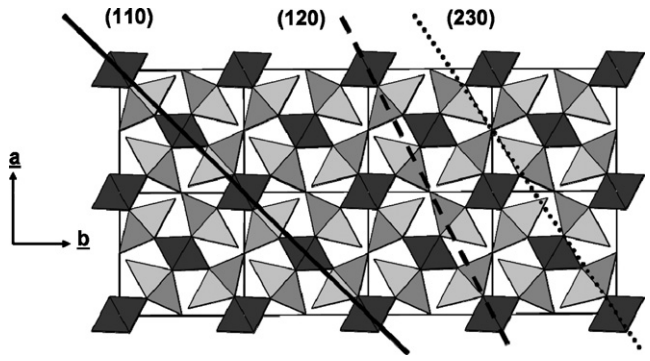

Fig. 9. The interaction of PDFs on (*h k 0*) mullite planes (excerpt only) with mullite coordination polyhedra as shown schematically in a [0 0 1] projection of the average 2/1 mullite structure (2 × 4 cells, positional parameters from [35]). Fully occupied octahedra are shown in dark gray, tetrahedra with (Si, Al) site occupancy ~0.8 in medium gray and tetrahedra with (Si, Al) site occupancy ~0.2 in light gray, respectively.

While the relative minima of the representation surface of the shear modulus provide a general guideline for suitable PDF orientations, supplementary constraints have to be considered before PDFs are likely to be retrieved in a shocked ceramic material. Firstly, it is well known from natural impact structures that the ratio of shocked-to-unshocked grains in a deformed volume increases with increasing grain size.[50] Secondly, control of the shock direction parallel to a crystallographic direction is less stringent in natural shock events as compared to a laboratory experiment thus introducing not only one, but several sets of PDF lamellae.[16] Moreover, in the fine-grained sintered mullite ceramic, the grain boundary-to-bulk volume ratio is much higher than for the coarse-grained mullite brick suggesting that high shear stresses necessary for PDF formation tend to relax in the mechanically rather soft grain boundaries. In the extreme case of very small grain sizes the applied mechanical field will rather correspond to a hydrostatic pressure state (no shear components) instead of an uniaxial stress field. In conclusion, these findings suggest that very fine-grained synthetic starting materials may fail to produce PDFs even at a sufficiently high shock level. This grain size effect is demonstrated in Fig. 6 for the fine-grained mullite ceramic upon shock loading at 35 GPa. Prior to dynamic compression the average grain size was of the order of 1 μm. Instead of PDF formation, thermal decomposition of mullite grains defined the only shock response mechanism yielding textured clusters of corundum microcrystals embedded in a continuous amorphous SiO_2 phase, in agreement with shock-induced thermal decomposition of andalusite and sillimanite.[51–53] No evidence for stishovite formation was found in this experiment.

The present study suggests that shock-induced amorphization via PDFs and thermal decomposition of mullite should be considered as complementary response mechanisms to shock loading and appreciated as a totality. While nucleation of PDFs is a sensitive function of original grain size and grain orientation relative to the shock direction, thermal decomposition of mullite only relies on high post-shock temperatures and can superimpose its effects on any shock-induced microstructure.

5. Conclusions

This research provided detailed insight into the unique response of mullite to dynamic compression in the laboratory. The two principal shock-induced transformation mechanisms of mullite including (i) PDFs, and (ii) thermal decomposition were evaluated for both, polycrystalline and single crystal mullite starting materials. At shock pressures exceeding 35 GPa both transformation mechanisms may occur within the same specimen.

Experimental PDF lamellae were shear-induced and formed parallel to densely packed $\{h\,k\,0\}$type-prism planes in mullite. PDFs in mullite were correlated to the relevant shock-wave directions via Mohr's circle. Orientation of PDFs in mullite was in good agreement with PDFs reported from sillimanite, mullite's close structural relative. Corundum crystals present as minor constituents in the mullite brick starting material, exhibited intensive twinning on the basal planes. High post-shock temperatures gave rise to thermal decomposition of mullite characterized by a corundum plus amorphous silica phase assemblage. No stishovite was observed. Even at sufficiently high shock levels no PDFs were obtained from a very fine-grained sintered mullite ceramic emphasizing the significance of the grain size of the starting material.

The crystallographic orientation of experimental PDFs can reasonably be explained via the anisotropy of the shear modulus in mullite. PDFs parallel to $\{1\,2\,0\}$, $\{2\,3\,0\}$ and $\{1\,1\,0\}$ planes match the relative minima of the representation surface of the shear modulus $G(l)$ in the $(0\,0\,1)$ section. These planes held a relative high density of $[AlO_6]$ octahedra. As the softest structural units in the mullite structure the octahedra are foremost affected by high shear stresses acting at $\pm 45^\circ$ off the main shock direction ([0 0 1] mullite in most cases). Due to the lack of data on the pressure dependence of the elastic stiffness coefficients, this approach remains qualitative. Nevertheless, it is well suited to identify possible soft modes in the shear deformation characteristics of mullite and predict PDF orientations which may be inaccessible for experimental reasons.

Appendix A. Deriving the anisotropy of elasticity for orthorhombic crystals (mullite)

Analytical expressions for the orientation dependence of the rigidity (shear) modulus G including Young's modulus E (as well as the reciprocals $1/G$ and $1/E$) for the general triclinic case were derived by Voigt[54] employing the matrix notation for the forth-rank elasticity tensors. Nowadays Voigt's matrix notation is widely adopted in crystal physics.[55,56] Voigt introduced factors of 2 or 4 in the definition of specific compliance matrix elements s_{ij} (two indices) which are related to corresponding tensor components s_{ijkl} (four indices): $s_{i,j} \leftrightarrow s_{iijj}$; $s_{i,9\text{-}k\text{-}l} \leftrightarrow 2{\cdot}s_{iikl}$; $s_{9\text{-}i\text{-}j,9\text{-}k\text{-}l} \leftrightarrow 4{\cdot}s_{ijkl}$ (known as multiplicity rule). As a consequence, all equations in matrix notation adopt the same compact form as in the corresponding tensor notation, including the inversion relation between c_{ij} and s_{ij} ($s_{ij} = {c_{ij}}^{-1}$).

Analytical expressions for $1/G$ (and $1/E$) using Voigt's matrix notation were published in 1950 by Schmid and Boas[57] for the cubic and hexagonal systems, and by Boas and Mackenzie[58] for the cubic, hexagonal, trigonal, and tetragonal crystal systems. In his book Nye[54] gave a summary of the expressions for $1/E$ for all crystal systems. In 1938 Wooster[59] published expressions $1/G$ (and for $1/E$) for the cubic, hexagonal, trigonal, and orthorhombic systems applying his matrix notation. (It should be noticed, that in contrast to Voigt, Wooster introduced a different matrix notation by relating all tensor components s_{ijkl} unmodified to the corresponding matrix elements s_{ij}, that is without introducing factors of 2 or 4. This fact has to be taken into account when comparing formulas and numerical values in the literature.)

The relevant formula for $1/G$, the reciprocal of the shear modulus in the orthorhombic crystal system (mullite), is listed below (Eq. (1)) utilizing Voigt's matrix notation convention with nine independent elastic stiffnesses c_{ij} or elastic compliances s_{ij} (s_{11}, s_{22}, s_{33}, s_{44}, s_{55}, s_{66}, s_{12}, s_{13}, s_{23}), respectively. The representation surfaces of the shear modulus G as displayed in Figs. 7a–c have been calculated from this approach.

$$\begin{aligned}\frac{1}{G} &= \frac{s'_{44} + s'_{55}}{2} \\ &= l_1^4 \frac{1}{2}(s_{55} + s_{66}) + l_2^4 \frac{1}{2}(s_{44} + s_{66}) + l_3^4 \frac{1}{2}(s_{44} + s_{55}) \\ &\quad + l_2^2 \cdot l_3^2 \left[2{\cdot}(s_{22} + s_{33} - 2 \cdot s_{23}) + \frac{1}{2}(s_{55} + s_{66} - 2 \cdot s_{44})\right] \\ &\quad + l_1^2 {\cdot} l_3^2 \left[2 \cdot (s_{11} + s_{33} - 2 \cdot s_{13}) + \frac{1}{2}(s_{44} + s_{66} - 2 \cdot s_{55})\right] \\ &\quad + l_1^2 {\cdot} l_2^2 \left[2 \cdot (s_{11} + s_{22} - 2 \cdot s_{12}) + \frac{1}{2}(s_{44} + s_{55} - 2 \cdot s_{66})\right]\end{aligned} \tag{1}$$

For completeness, the corresponding formula for $1/E$, the reciprocal of Young's modulus in orthorhombic systems is given by

$$\begin{aligned}\frac{1}{E} &= S'_{33} \\ &= l_1^4 \cdot s_{11} + l_2^4 \cdot s_{22} + l_2^4 s_{33} + l_2^2 \cdot l_3^2 \cdot (2 \cdot s_{23} + s_{44}) \\ &\quad + l_1^2 \cdot l_3^2 \cdot (2 \cdot s_{13} + s_{55}) + l_1^2 \cdot l_2^2 \cdot (2 \cdot s_{12} + s_{66})\end{aligned} \tag{2}$$

References

1. Richet, P. and Gillet, P., Pressure-induced amorphization of minerals: a review. *Eur. J. Miner.*, 1997, **9**, 907–933.
2. Langenhorst, F. and Hornemann, U., Shock experiments on minerals: basic physics and techniques. In *Mineral Behavior at Extreme Conditions. EMU Notes in Mineralogy 7, Chapter 15*, ed. R. Miletich. Eötvös University Press, Budapest, 2005, pp. 357–387.
3. Stoeffler, D., Keil, K. and Scott, E. R. D., Shock metamorphism of ordinary chondrites. *Geochim. Cosmochim. Acta*, 1991, **55**, 3845–3867.
4. Bischoff, A. and Stoeffler, D., Shock metamorphism as a fundamental process in the evolution of planetary bodies: information from meteorites. *Eur. J. Miner.*, 1992, **4**, 707–755.

5. Leroux, H., Microstructural shock signatures of major minerals in meteorites. *Eur. J. Miner.*, 2001, **13**, 253–272.
6. Murr, L. E., Residual microstructure–mechanical property relationship in shock-loaded metals and alloys. In *Shock Waves and High Strain Rate Phenomena in Metals*, ed. M. A. Meyers and L. E. Murr. Plenum Press, New York, 1981, pp. 607–673.
7. Sharma, S. and Sikka, S. K., Pressure induced amorphization of materials. *Progress in Materials Science*, 1996, **40**, 1–77.
8. Shih, C. J., Meyers, M. A., Nesterenko, V. F. and Chen, S. J., Damage evolution in dynamic deformation of silicon carbide. *Acta Mater.*, 2000, **48**, 2399–2420.
9. Hoenig, C. L. and Yust, C. S., Explosive compaction of AlN, amorphous Si_3N_4, boron and Al_2O_3 ceramics. *Ceram. Bull.*, 1981, **60**, 1175–1224.
10. Beauchamp, E. K., Carr, M. J. and Graham, R. A., Plastic deformation in alumina by explosive shock loading. *J. Am. Ceram. Soc.*, 1985, **68**, 696–699.
11. Hirai, H., Ohwada, T. and Kondo, K., Shock compression of graphite materials bearing different microtextures and their relations to diamond transition. *J. Mater. Res.*, 1995, **10**, 175–182.
12. Langenhorst, F., Shock metamorphism of some minerals: basic introduction and microstructural observations. *Bulletin of the Czech Geological Survey*, 2002, **77**, 265–282.
13. Müller, W. F. and Hornemann, U., Shock-induced planar deformation structures in experimentally shock-loaded olivines and in olivines from chondritic meteorites. *Earth Planet. Sci. Lett.*, 1969, **7**, 251–264.
14. Nicolas, A. and Poirier, J. P., *Crystalline Plasticity and Solid State Flow in Metamorphic Rocks*. Wiley, New York, 1976.
15. Leroux, H., Doukhan, J. C. and Langenhorst, F., Microstructural defects in experimentally shocked diopside: a TEM characterization. *Phys. Chem. Miner.*, 1994, **20**, 521–530.
16. Ashworth, J. R. and Schneider, H., Deformation and transformation in experimentally shock-load quartz. *Phys. Chem. Miner.*, 1985, **11**, 241–249.
17. Schneider, H., Shock-induced mechanical deformation in biotites from crystalline rocks of the Ries Crater (Southern Germany). *Contrib. Miner. Petrol.*, 1972, **37**, 75–85.
18. Born, M. and Huang, K., *Dynamical Theory of Crystal Lattices*. Oxford University Press, 1954.
19. Fedorov, F. I., *Theory of Elastic Waves in Crystals*. Plenum Press, New York, 1968.
20. Langenhorst, F., Shock experiments on pre-heated α- and β-quartz: II. X-ray and TEM investigations. *Earth Planet. Sci. Lett.*, 1994, **128**, 683–698.
21. Goltrant, O., Leroux, H., Doukhan, J. C. and Cordier, P., Formation mechanism of planar deformation features in naturally shocked quartz. *Phys. Earth Planet. Inter.*, 1992, **74**, 219–240.
22. Goltrant, O., Cordier, P. and Doukhan, J. C., Planar deformation features in shocked quartz: a transmission electron microscopy investigation. *Earth Planet. Sci. Lett.*, 1991, **106**, 103–115.
23. Langenhorst, F., Poirier, J. P., Deutsch, A. and Hornemann, U., Experimental approach to generate shock veins in single crystal olivine by shear melting. *Meteoritics Planet. Sci.*, 2002, **37**, 1541–1553.
24. Stöffler, D., Glassed formed by hypervelocity impact. *J. Non-cryst. Solids*, 1984, **67**, 465–502.
25. Hemley, R. J., Jephcoat, A. P., Mao, H. K., Ming, L. C. and Manghnan, M. H., Pressure-induced amorphization of crystalline silica. *Nature*, 1988, **374**, 52–54.
26. Clarke, D. R., Knoll, M. C., Kirchner, P. D., Cook, R. F. and Hockey, B. J., Amorphization and conductivity of silicon and germanium induced by indentation. *Phys. Rev. Lett.*, 1988, **60**, 2156–2159.
27. Schmücker, M., Schneider, H. and Kriven, W. M., Indentation-induced amorphization in mullite single crystals. *J. Am. Ceram. Soc.*, 2003, **86**, 1821–1822.
28. Bourne, N. K., Millet, J. C. F., Chen, M., Cauley, J. W. and Dandeka, D. P., On the Hugoniot elastic limit in polycrystalline alumina. *J. Appl. Phys.*, 2007, **102**, doi:10.1063/1.2787154.
29. Yust, C. S. and Harris, L. A., Observation of dislocations and twins in explosively compacted alumina. In *Shock Waves and High Strain Rate Phenomena in Metals*, ed. M. A. Meyers and L. E. Murr. Plenum Press, New York, 1981, pp. 881–894.
30. Wang, Y. and Mikkola, D. E., $\{0001\}\ \langle 1\,0\,\bar{1}\,0\rangle$ slip and basal twinning in sapphire single crystals shock-loaded at room temperature. *J. Am. Ceram. Soc.*, 1992, **75**, 3252–3256.
31. Stöffler, D., Shock deformation of sillimanite from the Ries Crater, Germany. *Earth Planet. Sci. Lett.*, 1970, **19**, 115–120.
32. Robertson, P. B. and Plant, A. G., Shock metamorphism in sillimanite from the Haughton impact structure, Devon Island, Canada. *Contrib. Miner. Petrol.*, 1981, **78**, 12–20.
33. Henry, H. H. and Radley, E. G., On certain xenolithic tertiary minor inclusions in the island of Mull. *Q. J. Geol. Soc. London*, 1922, **78**, 229–260.
34. Sadanaga, R., Tokonami, M. and Takeuchi, Y., The structure of mullite $2Al_2O_3{\cdot}SiO_2$ and relationship with the structures of sillimanite and andalusite. *Acta Crystallogr.*, 1962, **15**, 65–68.
35. Angel, R. J. and Prewitt, C. T., Crystal structure of mullite: a re-examination of the average structure. *Am. Miner.*, 1986, **71**, 1476–1482.
36. Braue, W., Schneider, H. and Hornemann, U., Shock wave-induced formation of diaplectic glasses from mullite $2Al_2O_3{\cdot}SiO_2$ crystals: a TEM study. Proceedings of the conference of the American Institute of Physics topical group on shock compression of condensed matter. *AIP Conference Proceedings*, 1996, **370**, 725–728.
37. Kawai, N., Nakamura, K. G. and Kondo, K., High-pressure transition of mullite under shock pressure. *J. Appl. Phys.*, 2004, **96**, 4126–4130.
38. Kawai, N., Atou, T., Ito, S., Yubuta, K., Kikuchi, M., Nakamura, K. G. and Kondo, K., Aligned nanocrystalline fragmentation of mullite under shock loading. *Adv. Mater.*, 2007, **919**, 2375–2378.
39. Hildmann, B., Braue, W. and Schneider, H., Topotactic growth of α-alumina platelets on 2/1 mullite single crystal surfaces upon thermal decomposition of mullite in dry and wet atmospheres. *J. Eur. Ceram. Soc.*, 2008, **28**, 407–423.
40. Unemoto, K., Wentzcovitch, R. M., Baroni, S. and de Gironcoli, S., Anomalous pressure-induced transition(s) in ice XI. *Phys. Rev. Lett.*, 2004, **92**, 1–4, 105502.
41. Hildmann, B., Ledbetter, H., Kim, S. and Schneider, H., Structural control of elastic constants of mullite in comparison to sillimanite. *J. Am. Ceram. Soc.*, 2001, **84**, 2409–2414.
42. Schreuer, J., Hildmann, B. and Schneider, H., Elastic properties of mullite single crystals up to 1400 °C. *J. Am. Ceram. Soc.*, 2006, **89**, 1624–1631.
43. Vaughan, M. T. and Weidner, D. J., The relationship of elasticity and crystal structure in andalusite and sillimanite. *Phys. Chem. Miner.*, 1978, **3**, 133–144.
44. Yang, H., Hazen, R. M., Finger, L. W., Prewitt, C. T. and Downs, R. T., Compressibility and crystal structure of sillimanite, Al_2SiO_5, at high pressure. *Phys. Chem. Miner.*, 1997, **25**, 39–47.
45. Kawai, N., Atou, T. and Kikuchi, M., The amorphization and disproportionation of mullite $3Al_2O_3{\cdot}2SiO_2$ under shock compression. In *14th APS Topical Conference on Shock Compression of Condensed Matter. Abstract C6. 00003*, 2005.
46. Atou, T., Kawai, N., Nakamura, K. G., Kondo, K., Kikuchi, M., Ito, S. and Yubuta, K., TEM observation of disproportionation of mullite and sillimanite under shock compression. In *15th APS Topical Conference on Shock Compression of Condensed Matter. Abstract C4.00005*, 2007.
47. Kawai, N., Harada, Y., Yokoo, M., Atou, T., Nakamura, K. G. and Kondo, K., Dynamic deformation and fracture of mullite $3Al_2O_3{\cdot}2SiO_2$ ceramics under hypervelocity impact. *Intern. J. Impact Eng.*, 2008, **35**, 1612–1645.
48. Atou, T., Kawai, N., Nakamura, G., Kondo, K., Ito, K., Yubuta, K. and Kikuchi, M., TEM observation of disproportionation of mullite and sillimanite under shock compression. In *Proceedings of the Conference of the American Physical Society Topical Group on Shock Compression of Condensed Matter, 955*, 2007, pp. 143–146, doi:10.1063/1.2832994.
49. Levin, I. and Brandon, D., Metastable alumina polymorph: crystal structures and transition sequences. *J. Am. Ceram. Soc.*, 1998, **81**, 1995–2012.
50. Walzebuck, J. P., Engelhardt, v. and Shock, W., deformation of quartz influenced by grain size and shock direction: observations on quartz-plagioclase rocks from the basement of the Ries Crater, Germany. *Contrib. Miner. Petrol.*, 1979, **70**, 267–271.

51. Schneider, H., Deformation of shock-loaded andalusite studied with X-ray diffraction techniques. *Phys. Chem. Miner.*, 1979, **4**, 245–252.
52. Schneider, H. and Hornemann, U., The disproportionation of andalusite (Al_2SiO_5) to Al_2O_3 and SiO_2 under shock compression. *Phys. Chem. Miner.*, 1977, **1**, 257–264.
53. Schneider, H. and Hornemann, U., Shock-induced transformation of sillimanite powders. *J. Mater. Sci.*, 1981, **16**, 45–49.
54. Voigt, W., *Lehrbuch der Kristallphysik* (*2nd edition*). Teubner Publishing Company, Leipzig, Germany, 1928, p. 733–763.
55. Haussühl, S., *Kristallphysik*. Physik-Verlag, Weinheim, Germany, 1983.
56. Nye, J. F., *Physical Properties of Crystals*. Oxford University Press, 1985 [reprint of 1st edition 1957].
57. Schmid, E. and Boas, W., *Plasticity of Crystals*. F.A. Hughes, London, 1950.
58. Boas, W. and Mackenzie, J. K., Anisotropy in metals. In *Prog. Met. Phys.*, *2*, ed. B. Chalmers. Butterworth Scientific Publications, London, 1950, pp. 90–120.
59. Wooster, W. A., *A Text-book on Crystal Physics*. University Press, Cambridge, 1938.